ACS OMEGA

Open Access

http://pubs.acs.org/journal/acsodf

Article

Matrix Swelling-Induced Precracking in Graphene Woven Fabric for Ultrasensitive Strain Sensors

Ying Wu,*,§ Yaru Guo,§ Wenxing Li, Kangxin Kong, and Naisheng Jiang*

Cite This: *ACS Omega* 2025, 10, 3141−3152

Read Online

ACCESS | Metrics & More | Article Recommendations | Supporting Information

ABSTRACT: The growing demand for highly sensitive flexible strain sensors in applications such as wearable electronics, healthcare monitoring, and environmental sensing has driven the development of materials capable of detecting subtle deformations with high precision. Herein, we introduce a precracked strain sensor based on solvent-swollen graphene woven fabric/polydimethylsiloxane (sGWF/PDMS) composites, designed to achieve ultrahigh gauge factors (GFs) and enhanced responsiveness to minor deformations. By utilizing PDMS swelling to induce network microcracks within the graphene structure, the sGWF/PDMS composites exhibit substantially improved sensitivity compared to traditional graphene-based strain sensors. Systematic *in situ* SEM analyses reveal that these preexisting microcracks expand readily under minor strain, resulting in rapid resistance changes that underpin the high sensitivity achieved. With GFs reaching up to 82,378 at only 2.8% stretching strain, the sGWF/PDMS composites demonstrate excellent performance across various applications, including human motion detection such as monitoring pulses, eye blinks, and speech-related movements, as well as detecting environmental disturbances such as water surface ripples. These findings highlight matrix-swollen composites as a promising platform for high-sensitivity, low-strain detection, offering great potential for advancements in wearable electronics, environmental monitoring, and other precision sensing applications.

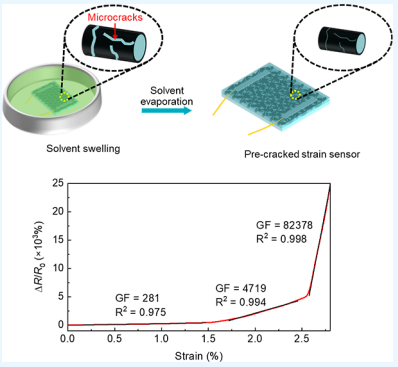

1. INTRODUCTION

The rapid advancement of flexible electronics has improved the demand for high-performance strain sensors capable of detecting subtle deformations with exceptional precision.[1,2] These sensors are critical across a diverse range of applications, including wearable healthcare monitoring, prosthetic implants, structural health monitoring, robotics, and environmental sensing, where high sensitivity, flexibility, durability, and reliability under repeated deformation cycles are important.[3−6] For instance, in healthcare applications, highly sensitive strain sensors enable real-time monitoring of physiological signals such as respiration rates, pulse waves, and muscle tension, providing valuable data for diagnostics and therapeutic guidance.[7−9] Additionally, strain sensors are promising in structural health monitoring, where they detect subtle vibrations in infrastructure, such as bridges, tunnels, and buildings, to identify early signs of misalignment or wear.[10−12] This capability enhances safety, minimizes maintenance costs, and prevents potential structural failures. However, achieving ultrahigh sensitivity, especially for low-strain or micro-deformation detection, remains a challenging task for most conductive materials.

Inspired by biological systems, where organisms such as scorpions, spiders, and mantises exhibit exceptional environmental sensitivity through slit sensilla, scientists have developed bioinspired precracked conductive networks to enhance strain sensor sensitivity.[10,13] This approach utilizes preformed cracks in conductive materials that open under minimal strain, enabling rapid and pronounced resistance changes. The sensing properties of these strain sensors are closely related to the morphology of preformed cracks, which can generally be categorized into two types: channel cracks and network cracks. Channel cracks, characterized by long and parallel cracks oriented perpendicular to the loading direction, open rapidly upon stretching, causing a sharp increase in resistance due to the immediate disruption of conductive pathways.[14,15] As a result, channel-crack-based strain sensors typically achieve ultrahigh sensitivity, with gauge factors approaching 10^5, at very small deformations (<5%).[7,16] However, their design and fabrication demand meticulous attention and precise control to achieve consistent performance. In contrast, network cracks consist of shorter, randomly oriented, and interconnected cracks that propagate in a curved manner along the stretching direction. This morphology maintains continuous conductive pathways even under high tensile strains, enabling network-crack-based strain sensors to

Received: November 15, 2024
Revised: December 17, 2024
Accepted: December 19, 2024
Published: January 14, 2025

https://doi.org/10.1021/acsomega.4c10403
ACS Omega 2025, 10, 3141−3152

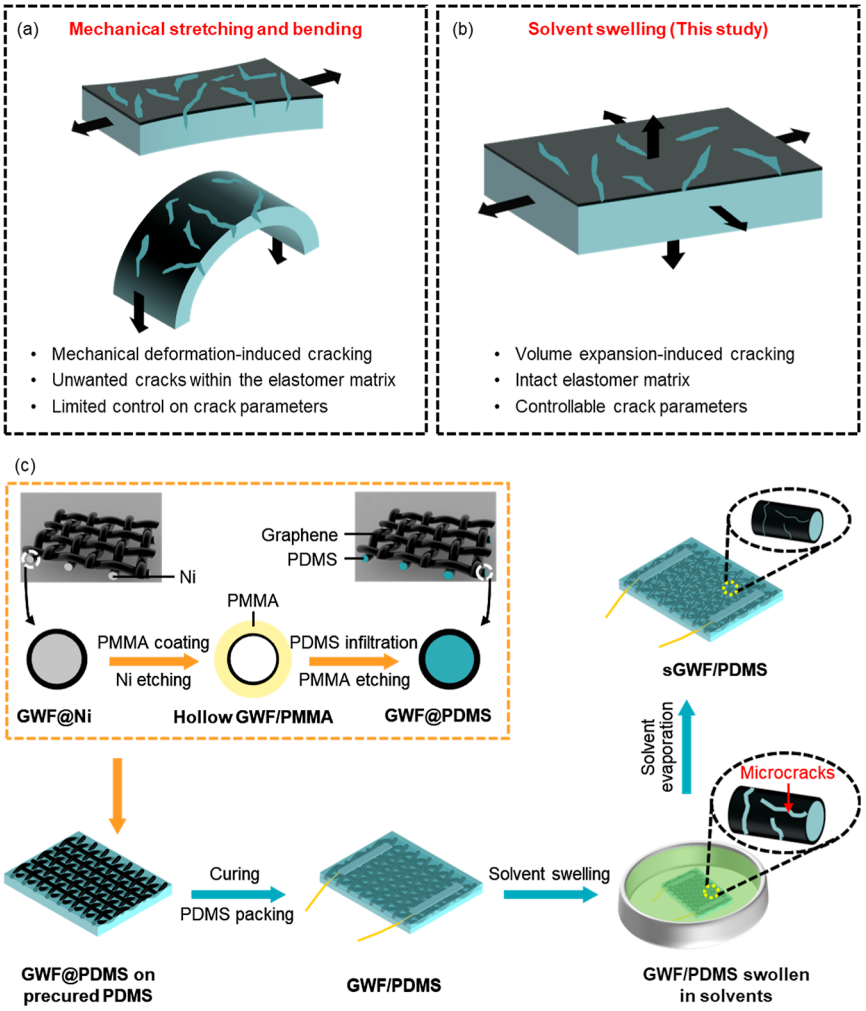

Figure 1. Conceptual design and fabrication process. (a) Mechanical stretching and bending for fabricating precracked strain sensors. (b) Polymer matrix swelling for fabricating precracked strain sensors. (c) Schematic illustrations of the fabrication process for sGWF/PDMS strain sensors.

support a broader strain range (exceeding 100%) but with relatively lower sensitivity.[7,16] Although network-crack-based sensors present a favorable balance between sensitivity and stretchability, it is worth exploring the possibility of network crack-based strain sensors for ultrasensitive sensing, as they offer a fabrication process that is both simpler and more suitable for practical applications.

Several techniques have been developed to introduce microcracks in conductive networks, including mechanical stretching, bending, laser ablation, and template-directed cracking.[15,17,18] These methods vary in scalability, complexity, and control over crack parameters. For example, laser ablation and template-directed cracking are more effective in creating channel cracks with well-defined crack parameters.[15,17,18] In comparison, mechanical stretching and bending are simpler methods that can generate both channel and network cracks but are limited in controlling crack parameters precisely. Moreover, the high-density precracks required for sensitive applications often necessitate extensive stretching or bending, which can lead to undesirable cracking within the elastomer matrix (Figure 1a), reducing sensor durability.[19,20] Such limitations underscore the need for precise and scalable methods to achieve controlled network cracks in strain sensors, thus fully leveraging their potential for ultrasensitive strain detection.

In this study, we introduce a facile cracking technique based on solvent swelling of the elastomer matrix, facilitating the fabrication of precracked conductive networks while maintaining matrix integrity (Figure 1b). By carefully controlling the swelling of polydimethylsiloxane (PDMS) with various solvents, we induce network cracks within a graphene woven fabric (GWF) skeleton fully infiltrated with PDMS, resulting in swollen GWF/PDMS (sGWF/PDMS) composites. As the PDMS swelling ratio increases, which leads to higher crack density in the GWF network, the sensitivity of the sGWF/PDMS composites also increases, though at the cost of reduced strain range. At an optimized swelling ratio of 1.59, the sGWF/PDMS composite achieves an exceptionally high gauge factor (GF) of 82,378 at only 2.8% strain, surpassing the sensitivity of conventional channel-crack-based sensors. This remarkable sensitivity to low-strain deformations makes the sGWF/PDMS composite particularly effective for precise human motion detection and environmental sensing applications. Our findings open new possibilities for designing precracked strain sensors, advancing the development of highly sensitive strain sensors for applications requiring the detection of subtle deformations.

2. EXPERIMENTAL SECTION

2.1. Preparation of sGWF/PDMS Composites. The fabrication process of sGWF/PDMS composites is schemati-

https://doi.org/10.1021/acsomega.4c10403
ACS Omega 2025, 10, 3141−3152

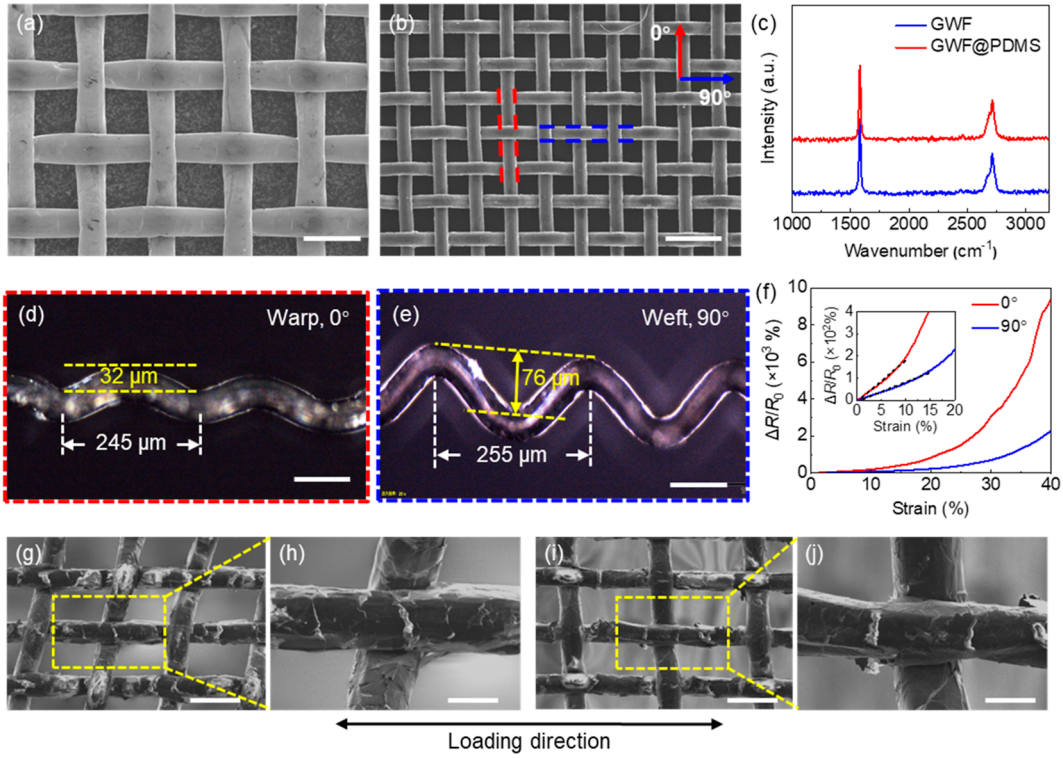

Figure 2. SEM images of (a) freestanding GWF and (b) GWF@PDMS. (c) Raman spectrum of GWF and GWF@PDMS. Optical images of the (d) warp and (e) weft wires, with yellow and white dashes indicating the double amplitude and the wavelength. (f) Normalized resistance changes of GWF@PDMS stretched along different directions. SEM images of GWF@PDMS at 40% strains stretched along the (g,h) 0° and (i,j) 90° directions. Scale bars (a,d,e) 100 μm, (b) 200 μm (g,i) 200 μm, and (h,j) 500 μm.

cally illustrated in Figure 1c. Graphene was synthesized on a nickel woven fabric (NiWF) substrate using chemical vapor deposition (CVD) technique.[21,22] Rectangular NiWFs (200 mesh, Hebei Chaochuang Metal Mesh Co., Ltd.) measuring 10 cm in length and 5 cm in width were first cleaned by ultrasonication in acetone (Sinopharm Chemical Reagent Co., Ltd.) for 60 min, followed by thorough rinsing with deionized water and drying overnight. Subsequently, the NiWF was heated to 1000 °C in a CVD furnace (OTF-1200X-II-80-SL, Hefei Kejing Materials) under a gas mixture of argon (Ar) and hydrogen (H_2). After a 10 min annealing period, methane (CH_4) was introduced into the CVD system for 20 min to provide the carbon source for graphene growth.[23] The oven was then rapidly cooled to room temperature to form the graphene woven fabric on nickel (GWF@Ni).

After graphene growth, the GWF@Ni was coated with poly(methyl methacrylate) (PMMA, Adamas) and immersed in 1 M hydrochloric acid (Sinopharm Chemical Reagent Co., Ltd.) to etch away the nickel substrate, obtaining hollow GWF/PMMA structures. A polydimethylsiloxane (PDMS, Dow Corning) solution with a base prepolymer-to-curing-agent ratio of 10:1 was infiltrated into the hollow graphene channels under vacuum assistance. After curing PDMS at 80 °C for 2 h, PMMA was removed using acetone (Sinopharm Chemical Reagent Co., Ltd.) at 40 °C for 5 times, yielding PDMS-filled GWF (GWF@PDMS).

To fabricate sGWF/PDMS composite strain sensors, a rectangle GWF@PDMS, measuring 20 mm in length and 5 mm in width, was partially embedded within a precured PDMS substrate that was fabricated by heating the PDMS mixture at 80 °C for 3 min. Copper wires were attached to both sides of the GWF@PDMS using silver pastes, followed by encapsulating with PDMS to prevent graphene delamination during the swelling and deformation processes, thereby ensuring the stability and consistency of sensors. After curing at 80 °C for 2 h, GWF/PDMS composites were obtained. These composites were then immersed in various organic solvents which have different PDMS-solvent interaction parameters,[24] including *n*-hexane (Sinopharm Chemical Reagent Co. Ltd.), ethyl acetate (Sinopharm Chemical Reagent Co. Ltd.), acetone (Sinopharm Chemical Reagent Co. Ltd.), and their mixtures at the room temperature for 10 min, to induce PDMS swelling and generate microcracks within the graphene network. PDMS exhibits minimal swelling in acetone (near zero), moderate swelling in ethyl acetate (1.25), and the highest swelling in *n*-hexane (1.79). By mixing these solvents and adjusting their volumetric ratios, we obtained a broad range of PDMS swelling ratios from 0.23 to 1.79, with details listed in Table S1. The volumetric expansion and modulus mismatch between graphene and PDMS during swelling induce the formation of microcracks within the graphene structure. By precisely controlling the swelling ratio of the PDMS matrix, the crack density in the graphene can be effectively regulated. After solvent evaporation, the composite returned to its original dimensions, obtaining swollen GWF/PDMS (sGWF/PDMS) composites. The sGWF/PDMS composites with varying swelling ratios were designated as Q_x-sGWF/PDMS, where Q_x denotes the swelling ratio, defined as the rate of volume expansion of PDMS relative to the original volume.

2.2. Optical Microscopy. The swelling behavior of sGWF/PDMS composites was observed using an optical microscope (Olympus, BX53MTRF-S) in transmission mode. Due to the transparency of PDMS and the opacity of GWFs,

https://doi.org/10.1021/acsomega.4c10403
ACS Omega 2025, 10, 3141−3152

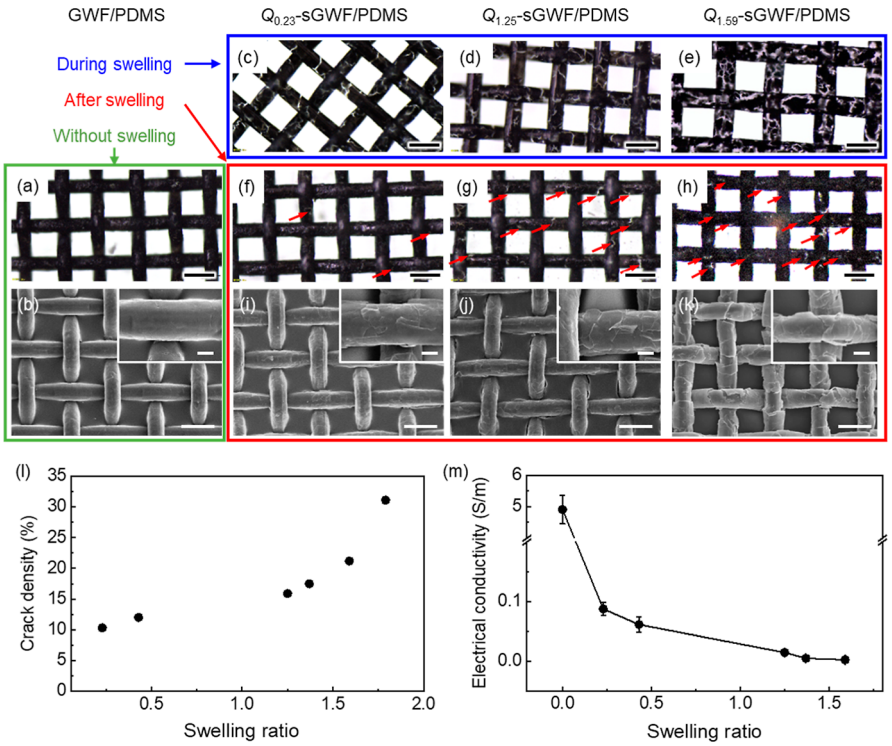

Figure 3. (a) Optical and (b) SEM images of GWF/PDMS composite. Optical images of sGWF/PDMS composites during swelling, with PDMS swelling ratios of (c) 0.23, (d) 1.25, and (e) 1.59. Optical images of the dried sGWF/PDMS composites after different ratios of swelling: (f) 0.23, (g) 1.25, and (h) 1.59. SEM images of partially embedded sGWF/PDMS composites after swollen by varying ratios: (i) 0.23, (j) 1.25, and (k) 1.59 (l) Crack density of graphene as a function of PDMS swelling ratio. (m) Electrical conductivity of sGWF/PDMS composites as a function of PDMS swelling ratio. Red arrows indicate microcracks within the graphene channels. Scale bars (a–k) 100 μm; insets in (b,i–k) 20 μm.

the light regions observed under optical microscopy indicated cracks introduced by PDMS swelling.

2.3. Scanning Electron Microscopy. The morphologies of GWFs, GWF/PDMS, and sGWF/PDMS composites were characterized using field-emission scanning electron microscopy (SEM) (Hitachi, SU-1510). Additionally, the *in situ* structural evolution of the composite sensors under tensile deformation was analyzed using an SEM (Merlin Compact, Zeiss, Germany) equipped with an automatic uniaxial tensile platform (Deben, MTEST 2000ES).

2.4. Raman Spectroscopy. The crystalline structure of GWFs, both before and after PDMS infiltration, was analyzed using Raman spectroscopy (WITec Alpha 300RA, WITec, Germany) with a 50× objective lens and an Ar laser with a wavelength of 532 nm.

2.5. Electromechanical Measurements. The strain-sensing performance of the composites was evaluated by fixing the samples, with an aspect ratio of 3, onto a material testing machine (HF-9002, Jiangsu Ligao Testing Equipment Co., LTD, China). Resistance changes during deformation were recorded using an LXI data logger switch unit (Keysight 34401A). The strain-sensing properties of sensors were quantified using the normalized resistance change ($\Delta R/R_0$), where R_0 is the initial resistance and ΔR is the real-time resistance change relative to the original value. The GFs were determined by the ratio of normalized resistance change and strain.

2.6. Measurement of Swelling Ratio. The swelling ratio, Q, of PDMS in various solvents was determined by the equation $Q = (V - V_0)/V_0$, where V and V_0 are the swollen and original volumes of PDMS, respectively. To measure the swelling ratio, a rectangular PDMS film with an initial volume V_0 was immersed in different solvents for 10 min, after which the swollen volume V was determined by measuring the side lengths of the film while still immersed in solvents.

3. RESULTS AND DISCUSSION

3.1. Optimization of the GWF@PDMS. The microstructure of the CVD-grown freestanding GWF is shown in Figure 2a, exhibiting a well-organized network of orthogonally interconnected hollow graphene channels. These channels, which are a direct inheritance from the original NiWF, are retained after the nickel substrate is removed, yielding a freestanding GWF that preserves the integrity of the original woven architecture.[25] Similarly, the woven structure of the GWF remains intact for GWF@PDMS (Figure 2b). The integration of PDMS confers elasticity to the composite, allowing it to endure substantial tensile strain up to 100% (Figure S1). To investigate the impact of PDMS infiltration on the crystalline structure of the GWF, we conducted Raman spectroscopy before and after the infiltration process. As shown in Figure 2c, the Raman spectra of both the pristine GWF and the GWF@PDMS exhibit two principal peaks: the G-band (~1580 cm^{-1}), associated with the in-plane vibrations of sp^2 carbon atoms, and the 2D-band (~2700 cm^{-1}), indicative of the layered graphene structure. The absence of D-band (~1350 cm^{-1}) in both spectra suggests that the GWF exhibits minimal defects, implying that the PDMS infiltration does not disrupt the graphene lattice.[26,27]

The graphene channels within the GWFs exhibit a wavy configuration, a feature inherited from the woven structure of the original nickel woven fabric. As shown in Figure 2d,e, the

https://doi.org/10.1021/acsomega.4c10403
ACS Omega 2025, 10, 3141−3152

wavelength of these waves is approximately 250 μm along both the warp (0°) and weft (90°) directions. However, a significant difference in amplitude is observed between the two directions: the warp direction exhibits a smaller amplitude (~16 μm), while the weft direction shows a larger amplitude (~38 μm). This contributes to the structural anisotropy of the GWF, which is expected to influence both the mechanical and electrical behavior of the material under tensile strain. To evaluate the strain sensing performance of the anisotropic GWF@PDMS, we measured the normalized resistance change ($\Delta R/R_0$) under uniaxial stretching along both the warp (0°) and weft (90°) directions. The results showed a linear response in the initial stages of deformation for both directions (Figures 2f and S2). When stretched along the 0° direction, GWF@PDMS demonstrates a linear resistance change region up to 10%, with a corresponding gauge factor of 19.5, indicating good sensitivity to small deformations. In contrast, when stretched along the 90° direction, the linear strain region extends to 15%, although the corresponding gauge factor is lower (9.0), suggesting lower sensitivity but a greater strain tolerance in this direction. For larger strain sensing, tensile deformation along the 0° direction results in a pronounced resistance increase of 928% at a strain of 40%, corresponding to a gauge factor of approximately 1000. This high gauge factor underscores its high sensitivity to strain when stretched along the warp direction, making it more suitable for high-sensitivity strain sensing applications. These findings indicate that the GWF@PDMS exhibits higher sensitivity when stretched along the 0° direction. Therefore, we conducted further investigations for strain sensing properties along in this orientation.

To understand the mechanism for higher sensitivity along the 0° direction, we observed structural evolution of the GWF skeleton using SEM (Figure 2g–j). Tensile strains primarily localize in the graphene channels that are aligned with the loading direction.[28] With the comparable strains for the woven structure stretched along both 0° and 90° direction (Figure S3), graphene structural evolution of the wavy warp and the weft differs. When GWF@PDMS is stretched along the 0° direction, the smaller amplitude of the warp limits its extension, resulting in larger localized strains in the warp graphene tubes. These strains induce the formation of microcracks within the graphene network (Figure 2g,h), which account for the marked increase in resistance. As the strain increases, these cracks propagate and, in some cases, result in the complete rupture of the conductive graphene channels, leading to the large resistance increments observed at higher strains. In contrast, when the material is stretched along the 90° direction, the larger amplitude of the weft provides greater structural deformability, reducing the strain experienced by the graphene tubes. Consequently, fewer microcracks are formed (Figure 2i,j), and those that do form propagate less readily, which explains the lower sensitivity and smaller resistance changes observed in this direction.

3.2. Morphologies of the sGWF/PDMS Composites. To investigate the effect of PDMS swelling on graphene networks, we systematically adjusted the PDMS swelling ratio using *n*-hexane, ethyl acetate, acetone, and their mixtures, obtaining a swelling ratio range of 0.23–1.79 (Table S1). The unmodified GWF/PDMS composites display intact graphene skeletons without microcracks (Figure 3a,b). Upon immersion in organic solvents, the PDMS matrix absorbs solvents, swells, and introduces microcracks within the graphene network (Figures 3c–e and S4). This crack formation is attributed to the mismatch in swelling and deformability between PDMS and graphene, as graphene remains unswollen in solvents and exhibits significantly lower deformability. As the swelling ratio increased, the number of microcracks in the sGWF/PDMS composites increased correspondingly, as evidenced by the light regions observed in the optical microscopy images (Figure 3c–e). Following the full evaporation of the solvents, the PDMS matrix returns to its original volume. However, the fractured graphene channels cannot recover to their original form, leaving residual microcracks within the network (red arrows in Figure 3f–h). These microcracks are directly related to the swelling ratio of the PDMS matrix: Larger swelling ratios result in denser microcracks (Figure 3i–k). Compared to the relatively smooth, continuous graphene morphology in the unswollen GWF/PDMS composite (Figure 3i), the graphene channels in the sGWF/PDMS composites show a cataphracted, wrinkled appearance (Figure 3j,k). Additionally, the roughness of the graphene channels increases with higher swelling ratios. Although cracks are introduced within the GWF skeleton, the PDMS matrix remains intact after a maximum swelling ratio of 1.79 involved in this study (Figure S4), eliminating the detrimental effect of matrix cracking on sensor durability.

To quantitatively investigate the graphene cracking induced by PDMS swelling, we analyzed the crack density, defined as the percentage of cracked area relative to the total area of the woven fabric skeleton,[29] of graphene in sGWF/PDMS composites based on optical microscopic images (Figures 3c–e and S4) using Image-Pro software. As shown in Figure 3l, the crack density increases with higher PDMS swelling ratios, ranging from approximately 10% to 31% as the swelling ratio rises from 0.23 to 1.79. The formation of microcracks significant influences the electrical conductivities of composites (Figure 3m). While the unswollen GWF/PDMS composite exhibits an electrical conductivity of approximately 5 S/m, the conductivity dramatically decreases to the order of 10^{-3} S/m in solvent-swollen composites. Moreover, higher swelling ratios lead to further reductions in electrical conductivity. The $Q_{1.79}$-sGWF/PDMS, having the highest swelling ratio, becomes electrically insulating due to the high crack density in the graphene skeleton (Figure S5).

3.3. Strain Sensing Properties. To investigate the influence of PDMS swelling on the strain-sensing properties of sGWF/PDMS composites, we measured resistance changes of composites with varying PDMS swelling ratios under tensile deformations (Figure 4a). It was found that higher PDMS swelling ratios, which correspond to greater volumetric expansion and elevated crack densities in the graphene network, lead to pronounced resistance variations under strain, though this is accompanied by a reduction in stretchability. Notably, the unswollen GWF/PDMS composite exhibits a high GF of approximately 9497 and a stretchability of up to 50% (Figure 4b), demonstrating its potential for applications requiring moderate deformation sensitivity. For composites exposed to a swelling ratio of 1.59 ($Q_{1.59}$-sGWF/PDMS), the GFs are significantly enhanced, especially at low strain levels, with GFs of approximately 281, 4719, and 82,378 across strain ranges of 0–1.5%, 1.5–2.5%, and 2.5–2.8%, respectively (Figure 4c). This notable increase in GF can be attributed primarily to the preexisting microcracks within the graphene framework, which intensify resistance changes in response to strain (*vide infra*). Besides, $Q_{1.59}$-sGWF/PDMS shows a detection limit of 0.01% strain (Figure S6). The low-strain

https://doi.org/10.1021/acsomega.4c10403
ACS Omega 2025, 10, 3141–3152

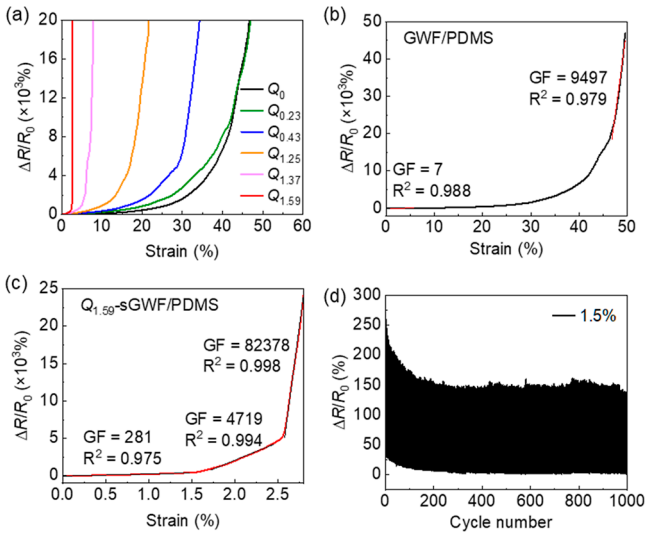

Figure 4. Electromechanical properties of sGWF/PDMS composite strain sensors. (a) Normalized resistance changes of sGWF/PDMS composites with varying swelling ratios as a function of applied tensile strain. Normalized resistance changes of (b) GWF/PDMS and (c) $Q_{1.59}$-sGWF/PDMS composites against tensile strains, with straight lines showing linear fittings for the determination of GFs. (d) Normalized resistance changes of $Q_{1.59}$-sGWF/PDMS composites during cyclic stretching to 1.5% strains.

GF of sGWF/PDMS composites with varying swelling ratios, corresponding to different crack densities in graphene, is presented in Figures S7 and S8. These results indicate that the sensitivity of the composites in the low-strain range increases with higher swelling ratios, which correlate with increased crack density. However, the stretchability and the first linear response range decrease with increasing crack density (Figure S9).

The stability of cyclic strain sensing is essential for practical sensor applications. To evaluate the durability of the sGWF/PDMS composites, we conducted cyclic resistance testing of $Q_{1.59}$-sGWF/PDMS at a maximum strain of 1.5% (Figure 4d). It was found that both maximum resistances under stretching and minimum resistance in the unstrained state decrease in the initial cycles; however, stable cyclic sensing performances are achieved after approximately 60 cycles. Similar stability was also observed in sGWF/PDMS composites prepared at other PDMS swelling ratios, including $Q_{0.23}$-sGWF/PDMS and $Q_{1.25}$-sGWF/PDMS (Figure S10), demonstrating robust durability across diverse sGWF/PDMS configurations. These findings indicate that PDMS matrix swelling is an effective strategy for producing highly sensitive and durable strain sensors, suitable for subtle deformation detection.

To evaluate the strain sensing properties of sGWF/PDMS composites, we compared GFs across various strain levels against other graphene-based strain sensors (Figure 5a). Conventional graphene-based strain sensors typically exhibit GFs below 10^4.[25,28,30−42] In particular, CVD-grown graphene foams, owing to their 3D interconnected and porous architectures, typically show low sensitivity, with GFs under 100 across strain ranges of 0−50% (depicted by blue hollow points in Figure 5a).[31,33,35] Conversely, GWFs, Conversely, GWFs, which possess a more planar interconnected structure, demonstrate lower deformation adaptability (represented by blue solid points), yielding higher GFs but reduced stretchability.[25,28,30,32] This configuration enables GWFs to achieve GFs around 580 at 6.2% strain.[32] Other CVD-grown graphene architectures, such as films,[34] braided belts,[36] and vertically aligned walls,[37] also exhibit low stretchability but only moderate GFs, showing approximately 5000 at 2% strain (blue half-hollow points). Additionally, reduced graphene oxide (rGO)-based strain sensors show tunable sensitivities, with GFs ranging from 10 to over 1000, and stretchability up to about 50%.[38−42] Comparatively, the sGWF/PDMS

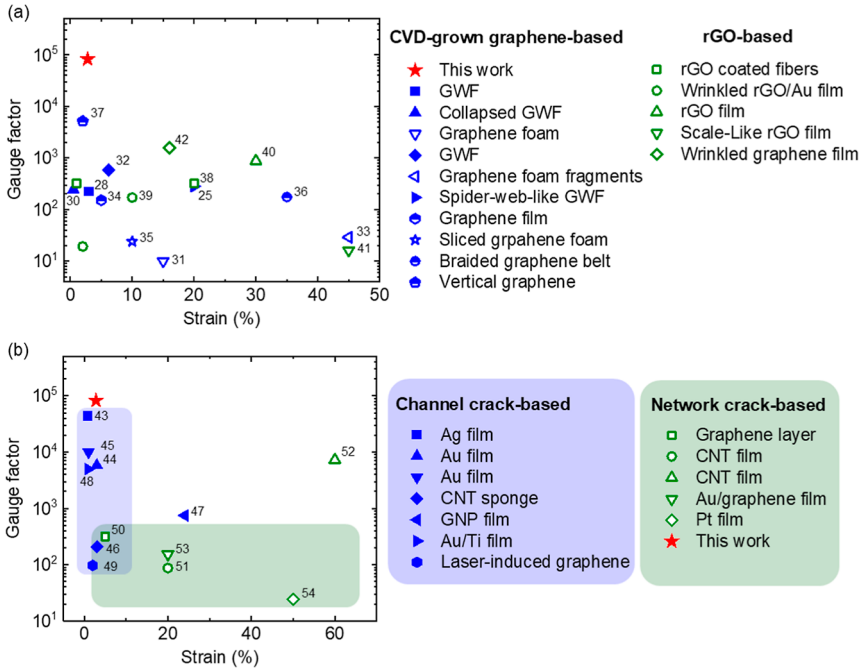

Figure 5. Comparison of strain sensing properties of sGWF/PDMS composites with various (a) graphene-based strain sensors,[25,28,30−42] and (b) precracked strain sensors.[43−54]

https://doi.org/10.1021/acsomega.4c10403
ACS Omega 2025, 10, 3141−3152

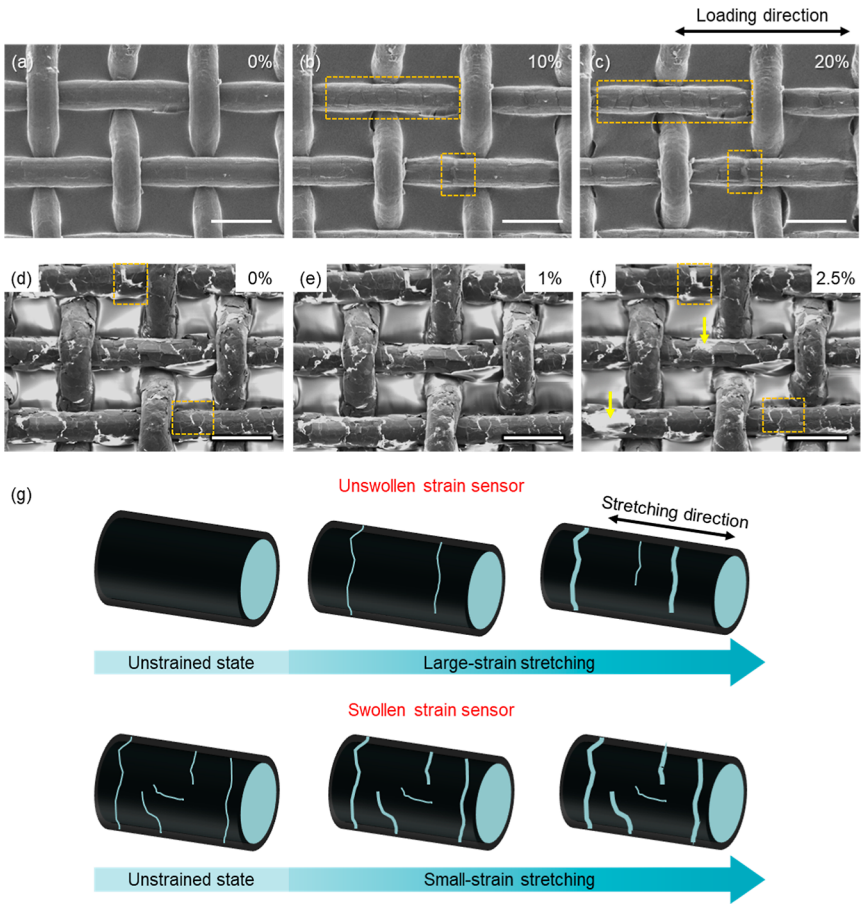

Figure 6. (a–c) *In situ* SEM images of GWF/PDMS under varying tensile strains. (d–f) *In situ* SEM images of $Q_{1.59}$-sGWF/PDMS at different tensile strains. Orange rectangles show regions of graphene cracking, while yellow arrows indicate graphene exfoliation from the PDMS matrix. (g) Schematic illustrations of the sensing mechanisms for sensors with and without PDMS swelling. Scale bars: 100 μm.

composites demonstrate remarkably high GFs, demonstrating their potential for applications that demand high sensitivity to minor deformations.

We further conducted a comparative analysis with various precracked sensors to get a more comprehensive insight into the sensing properties of sGWF/PDMS composites (Figure 5b). A comprehensive comparison of key performance parameters is summarized in Table S2, which includes gauge factors, strain levels, the first linear sensing range, and durability across different precracked strain sensors. Channel-crack-based strain sensors, characterized by elongated cracks perpendicular to the tensile direction within conductive materials, are known for their high sensitivity, achieving GFs exceeding 10^4 but with limited stretchability generally below 5%.[43−49] In contrast, network-crack-based sensors, which feature shorter and randomly oriented cracks, exhibit greater strain ranges (up to or beyond 100%) but typically lower GFs, generally below 10^4.[50−54] Our solvent-swelling-induced network-crack-based sGWF/PDMS sensor overcomes this limitation, achieving ultrahigh sensitivity (GF = 82,378) at subtle deformations (2.8% strain), not only significantly exceeding the sensitivity of other network-crack-based strain sensors but also surpassing that of channel-crack-based sensors. Moreover, this strain sensor also shows decent linear sensing capacity and durability. This extraordinary performance highlights its suitability for applications where extreme sensitivity to small deformations is essential.

To reveal the mechanism for the significantly enhanced sensitivity of sGWF/PDMS composites with PDMS swelling-induced cracks, we examined the structural evolution of graphene within both GWF/PDMS and sGWF/PDMS composites under tensile deformation using *in situ* SEM (Figure 6a–f). In the unstrained state, the GWF/PDMS composite displays a continuous, uncracked graphene framework (Figure 6a). However, microcracks initiate and propagate within the graphene channels aligned along the loading direction during stretching to 20% strain (Figure 6b,c), leading to a measurable increase in resistance. Additionally, at this high strain, graphene tubes perpendicular to the loading direction detach from the PDMS substrate due to weak van der Waals forces between graphene and PDMS, forming interfacial voids. These voids are readily deformable upon stretching, effectively mitigating strain on the graphene wefts and preserving their structural continuity.[55] In contrast, $Q_{1.59}$-sGWF/PDMS composites, swollen by a PDMS volume expansion ratio of 1.59, exhibit a highly cracked graphene network even in the absence of applied strain (Figure 6d). Upon stretching to 1% and 2.5% strains, these preexisted microcracks open further (highlighted in orange rectangles in Figure 6d–f), causing a rapid increase in resistance and thus contributing to the high sensitivity of the strain sensor. Furthermore, fractured graphene segments within graphene tubes along you loading direction detach from the PDMS matrix (yellow arrows in Figure 6f). Although the final $Q_{1.59}$-sGWF/PDMS sensors are encapsulated by PDMS for protecting the graphene skeleton

https://doi.org/10.1021/acsomega.4c10403
ACS Omega 2025, 10, 3141−3152

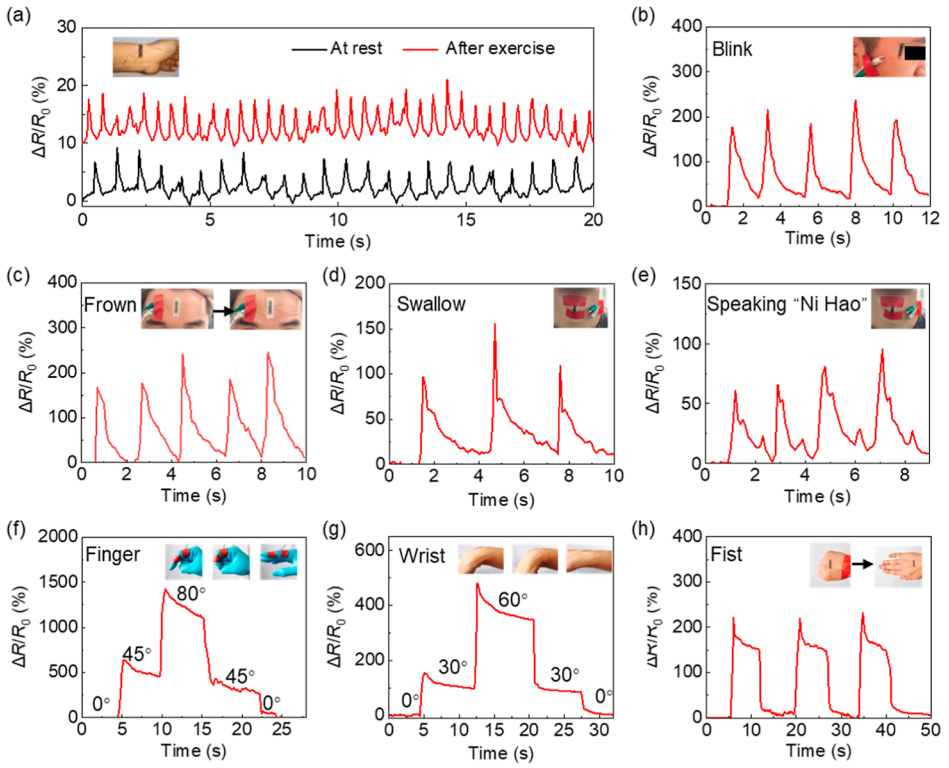

Figure 7. Demonstrated applications of sGWF/PDMS composites as strain sensors for detecting subtle deformations and human motions: (a) radial artery pulses at rest and postexercise; (b) eye blinking; (c) frowning; (d) swallowing; (e) words speaking of "Ni Hao"; (f) finger bending; (g) wrist bending; and (h) fist clenching. For clarity, the data in (a) was shifted vertically.

from exfoliation, the weak interfacial bonding in the swollen composite leaves these loosely connected graphene fragments vulnerable to further fracturing. Additional *in situ* SEM observations for $Q_{0.23}$-sGWF/PDMS (Figure S11) and $Q_{1.25}$-sGWF/PDMS (Figure S12) reveal the precrack density-dependent structural evolution for composites. These findings indicate that the preexisting cracks in the sGWF/PDMS composite are the primary factors driving their high sensitivity. The underlying mechanisms are schematically illustrated in Figure 6g. In unswollen composites, the intact conductive skeleton accommodates larger deformations before microcracks initiate and propagate, which results in moderate resistance increases and sensitivity. Conversely, the swollen composites with preexisting microcracks exhibit crack opening at minimal tensile strains, leading to a rapid resistance increase and enhanced sensitivity. This precrack-driven response in the sGWF/PDMS composites highlights their suitability for high-sensitivity strain sensing at low deformation levels.

3.4. Demonstrations of sGWF/PDMS Composites as Wearable Sensors. Leveraging the ultrahigh sensitivity of sGWF/PDMS composites, these materials exhibit good potential for strain sensors designed to monitor various human movements with high precision. When applied to different skin locations, these sensors provide real-time, accurate physiological monitoring. As shown in Figure 7a, a sensor attached to the radial artery detects pulse frequency variations both at rest and postexercise, maintaining high sensitivity in both conditions. When positioned at the outer corner of the eye, the sensor reliably records eye blinks, showing consistent resistances at open-eye states and increased resistances upon eye closure (Figure 7b). Similarly, when attached to the forehead, the sensor effectively detects facial skin contractions, as evidenced by increased resistance during frowning (Figure 7c). We further demonstrated its application in the monitoring of laryngeal prominence movements and speech, where normalized resistance patterns reflect the repetitive swallowing cycles (Figure 7d) and the repetitive speaking of "Ni Hao" (Figure 7e). The versatility of sGWF/PDMS is also confirmed in monitoring joint movement (Figure 7f,g) and skin extension (Figure 7h), underscoring its reliability across a diverse range of human motion detection scenarios.

The ultrahigh sensitivity of sGWF/PDMS composite sensors also enables effective monitoring of water surface disturbances, which is important for environmental sensing and alert systems. When floating on water with supportive plastic foam (Figure 8a), the sensor dynamically responds to water surface ripples. For instance, a gentle touch on the water surface generates ripples that the sensor detects as increases in resistance (Figure 8b and Video S1). As the ripples diminish over time, its resistance gradually returns to baseline in a fluctuating pattern. Figure 8c further demonstrates its responsiveness to external impacts on the water container, with each strike yielding immediate and notable resistance increases. These fluctuations correlate with strike frequency, indicating its capacity to track disturbance patterns consistently (Video S2). The sensor also exhibits resistance changes when objects are dropped into the water, with greater dropping heights (from 5 cm to 10, 15, and 20 cm) producing more pronounced ripples and corresponding larger maximum normalized resistance changes (Figure 8d and Video S3). Additionally, in windy environments, where timely detection can mitigate economic and safety risks, the sensor records resistance changes that correlate with wind intensity; gentle

https://doi.org/10.1021/acsomega.4c10403
ACS Omega 2025, 10, 3141−3152

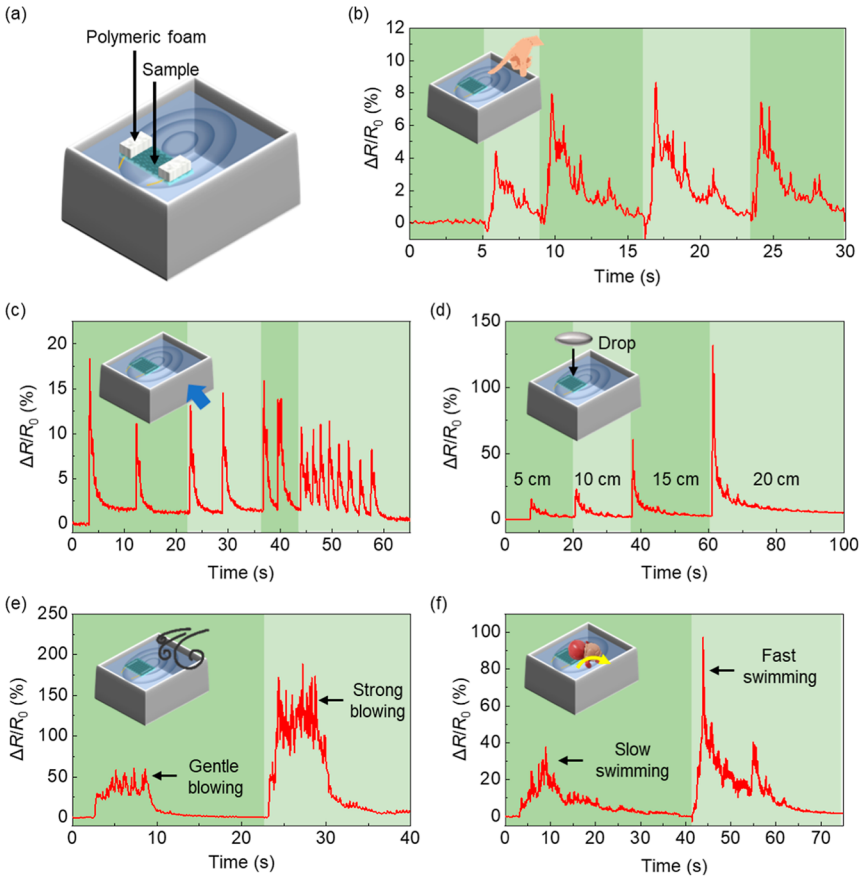

Figure 8. Applications of sGWF/PDMS composites for detecting water surface ripples. (a) Schematic illustration of the sensor floating on water. Normalized resistance changes of the sensor under various water surface disturbances caused by (b) finger touching, (c) striking, (d) object dropping, (e) blowing, and (f) toy turtle swimming.

winds induce minor resistance changes, while stronger gusts result in more pronounced resistance increases (Figure 8e and Video S4). Moreover, the sensor effectively detects continuous surface disturbances, such as those produced by a swimming object like a toy turtle (Figure 8f and Video S5). This wide range of applications confirms the adaptability and precision of the sGWF/PDMS composite sensor, highlighting its potential as a valuable tool for both human motion detection and environmental monitoring applications.

4. CONCLUSIONS

In conclusion, this study introduces the sGWF/PDMS composite as a highly sensitive and versatile strain sensor, ideal for both wearable applications and environmental monitoring. The unique structural features of these composites, particularly the preexisting microcracks within the graphene skeleton induced by PDMS swelling, coupled with an intact matrix following cracking treatment, are crucial to their ultrahigh sensitivity and excellent durability under subtle deformations. Notably, the rapid opening of these preexisting network microcracks enables the sGWF/PDMS composites to achieve a remarkable gauge factor of 82,378 at only 2.8% strain. The composites demonstrate great potential for monitoring various human movements and physiological signals, as well as detecting environmental disturbances such as water surface ripples. These findings highlight the effectiveness of matrix swelling as a cracking technique for the fabricating highly sensitive strain sensors, advancing the field of strain-sensing materials. We hope that this research will set the stage for the development of sensors that are highly sensitive, adaptive, and durable, making them suitable for a broad range of applications.

■ ASSOCIATED CONTENT

Supporting Information

The Supporting Information is available free of charge at https://pubs.acs.org/doi/10.1021/acsomega.4c10403.

Photos of GWF@PDMS composite, normalized resistance changes of GWF@PDMS, Optical microscopic images of GWF@PDMS stretched along different directions. Optical microscopic images and SEM images of $Q_{1.79}$-sGWF/PDMS during and after swelling, cyclic strain sensing properties of $Q_{0.23}$-sGWF/PDMS and $Q_{1.25}$-sGWF/PDMS, *in situ* SEM images of $Q_{0.23}$-sGWF/PDMS and $Q_{1.25}$-sGWF/PDMS during stretching, swelling ratios of PDMS in various solvents, comparison of strain sensing properties (PDF)

Demonstration of sGWF/PDMS composites for detecting water surface ripples caused by finger touching (MP4)

Demonstration of sGWF/PDMS composites for detecting water surface ripples caused by striking (MP4)

Demonstration of sGWF/PDMS composites for detecting water surface ripples caused by object dropping (MP4)

https://doi.org/10.1021/acsomega.4c10403
ACS Omega 2025, 10, 3141−3152

Demonstration of sGWF/PDMS composites for detecting water surface ripples caused by blowing (MP4)

Demonstration of sGWF/PDMS composites for detecting water surface ripples caused by turtle swimming (MP4)

AUTHOR INFORMATION

Corresponding Authors

Ying Wu − *Beijing Advanced Innovation Center for Materials Genome Engineering, School of Materials Science and Engineering, University of Science and Technology Beijing, Beijing 100083, China;* orcid.org/0000-0003-0674-2198; Email: wuying@ustb.edu.cn

Naisheng Jiang − *Beijing Advanced Innovation Center for Materials Genome Engineering, School of Materials Science and Engineering, University of Science and Technology Beijing, Beijing 100083, China; Institute of Materials Intelligent Technology, Liaoning Academy of Materials, Shenyang 110004, China;* orcid.org/0000-0002-3507-5219; Email: naishengjiang@ustb.edu.cn

Authors

Yaru Guo − *Beijing Advanced Innovation Center for Materials Genome Engineering, School of Materials Science and Engineering, University of Science and Technology Beijing, Beijing 100083, China*

Wenxing Li − *Beijing Advanced Innovation Center for Materials Genome Engineering, School of Materials Science and Engineering, University of Science and Technology Beijing, Beijing 100083, China*

Kangxin Kong − *Beijing Advanced Innovation Center for Materials Genome Engineering, School of Materials Science and Engineering, University of Science and Technology Beijing, Beijing 100083, China*

Complete contact information is available at: https://pubs.acs.org/10.1021/acsomega.4c10403

Author Contributions

[§]Y.W. and Y.G. contributed equally to this work. Y.W.: conceptualization, methodology, resources, writing - original draft, writing - review & editing, visualization, project administration, funding acquisition. Y.G.: validation, formal analysis, investigation, data curation, writing - original draft. W.L.: formal analysis, writing - original draft, visualization. K.K.: validation, formal analysis, investigation, data curation, visualization. N.J.: resources, writing - review & editing, supervision, project administration, funding acquisition. The manuscript was written through contributions of all authors. All authors have given approval to the final version of the manuscript.

Funding

This work was supported by the National Natural Science Foundation of China (Nos. 52002020, 52073025).

Notes

The authors declare no competing financial interest.

ACKNOWLEDGMENTS

The authors thank Xiao Li from the National Center for Materials Service Safety in the University of Science and Technology for assisting with *in situ* SEM measurements.

REFERENCES

(1) Shen, Z.; Liu, F.; Huang, S.; Wang, H.; Yang, C.; Hang, T.; Tao, J.; Xia, W.; Xie, X. Progress of flexible strain sensors for physiological signal monitoring. *Biosens. Bioelectron.* **2022**, *211*, 114298.

(2) Wang, J.; Liu, S.; Chen, Z.; Shen, T.; Wang, Y.; Yin, R.; Liu, H.; Liu, C.; Shen, C. Ultrasensitive electrospinning fibrous strain sensor with synergistic conductive network for human motion monitoring and human-computer interaction. *J. Mater. Sci. Technol.* **2025**, *213*, 213−222.

(3) Chen, Z.; Liu, S.; Kang, P.; Wang, Y.; Liu, H.; Liu, C.; Shen, C. Decoupled Temperature−Pressure Sensing System for Deep Learning Assisted Human−Machine Interaction. *Adv. Funct. Mater.* **2024**, 2411688.

(4) Yang, W.; Pan, D.; Liu, S.; Jia, G.; Wang, Y.; Liu, H.; Liu, C.; Shen, C. Multifunctional Wearable Conductive Nanofiber Membrane with Antibacterial and Breathable Ability for Superior Sensing, Electromagnetic Interference Shielding, and Thermal Management. *Adv. Funct. Mater.* **2024**, 2414811.

(5) Wang, Z.; Xing, D.; Yin, R.; Zhan, P.; Liu, C.; Shen, C.; Liu, H. Breathable and waterproof conductive cotton fabric pressure sensor with distinguished electrothermal and electromagnetic interference shielding performances. *Appl. Mater. Today* **2024**, *38*, 102256.

(6) Yang, W.; Liu, S.; Wang, Z.; Liu, H.; Pan, C.; Liu, C.; Shen, C. Bioinspired composite fiber aerogel pressure sensor for machine-learning-assisted human activity and gesture recognition. *Nano Energy* **2024**, *127*, 109799.

(7) Wang, W.; Liu, Y.; Ding, M.; Xia, T.; Gong, Q.; Zeng, X.; Cai, Z.; Hu, Y. From network to channel: Crack-based strain sensors with high sensitivity, stretchability, and linearity via strain engineering. *Nano Energy* **2023**, *116*, 108832.

(8) Sun, Z.; Yang, S.; Zhao, P.; Zhang, J.; Yang, Y.; Ye, X.; Zhao, X.; Cui, N.; Tong, Y.; Liu, Y.; et al. Skin-like ultrasensitive strain sensor for full-range detection of human health monitoring. *ACS Appl. Mater. Interfaces* **2020**, *12* (11), 13287−13295.

(9) Ai, J.; Wang, Q.; Li, Z.; Lu, D.; Liao, S.; Qiu, Y.; Xia, X.; Wei, Q. Highly stretchable and fluorescent visualizable thermoplastic polyurethane/tetraphenylethylene plied yarn strain sensor with heterogeneous and cracked structure for human health monitoring. *ACS Appl. Mater. Interfaces* **2024**, *16* (1), 1428−1438.

(10) Liu, L.; Niu, S.; Zhang, J.; Mu, Z.; Li, J.; Li, B.; Meng, X.; Zhang, C.; Wang, Y.; Hou, T.; et al. Bioinspired, omnidirectional, and hypersensitive flexible strain sensors. *Adv. Mater.* **2022**, *34* (17), 2200823.

(11) Goyal, D.; Pabla, B. The vibration monitoring methods and signal processing techniques for structural health monitoring: a review. *Arch. Comput. Method. E* **2016**, *23*, 585−594.

(12) Wang, Q.; Yao, Z.; Zhang, C.; Song, H.; Ding, H.; Li, B.; Niu, S.; Huang, X.; Chen, C.; Han, Z.; et al. A selective-response hypersensitive bio-inspired strain sensor enabled by hysteresis effect and parallel through-slits structures. *Nano-Micro Lett.* **2023**, *16* (1), 26.

(13) Kang, D.; Pikhitsa, P. V.; Choi, Y. W.; Lee, C.; Shin, S. S.; Piao, L.; Park, B.; Suh, K.-Y.; Kim, T.-i.; Choi, M. Ultrasensitive mechanical crack-based sensor inspired by the spider sensory system. *Nature* **2014**, *516* (7530), 222−226.

(14) Zhang, H.; Liu, D.; Lee, J. H.; Chen, H.; Kim, E.; Shen, X.; Zheng, Q.; Yang, J.; Kim, J. K. Anisotropic, wrinkled, and crack-bridging structure for ultrasensitive, highly selective multidirectional strain sensors. *Nano-Micro Lett.* **2021**, *13* (1), 122.

(15) Zhang, C.; Sun, J.; Lu, Y.; Liu, J. Nanocrack-based strain sensors. *J. Mater. Chem. C* **2021**, *9* (3), 754−772.

(16) Pu, J.-H.; Zhao, X.; Zha, X.-J.; Li, W.-D.; Ke, K.; Bao, R.-Y.; Liu, Z.-Y.; Yang, M.-B.; Yang, W. A strain localization directed crack control strategy for designing MXene-based customizable sensitivity and sensing range strain sensors for full-range human motion monitoring. *Nano Energy* **2020**, *74*, 104814.

(17) Zhou, Y.; Lian, H.; Li, Z.; Yin, L.; Ji, Q.; Li, K.; Qi, F.; Huang, Y. Crack engineering boosts the performance of flexible sensors. *View* **2022**, *3* (5), 20220025.

(18) Kim, Y.-N.; Lee, J.; Kang, S.-K. Ultrasensitive crack-based strain sensors: Mechanism, performance, and biomedical applications. *J. Mech. Sci. Technol.* **2022**, *36* (3), 1059−1077.
(19) Kim, T.; Hong, I.; Kim, M.; Im, S.; Roh, Y.; Kim, C.; Lim, J.; Kim, D.; Park, J.; Lee, S.; et al. Ultra-stable and tough bioinspired crack-based tactile sensor for small legged robots. *npj Flex. Electron.* **2023**, *7* (1), 22.
(20) Park, B.; Kim, J.; Kang, D.; Jeong, C.; Kim, K. S.; Kim, J. U.; Yoo, P. J.; Kim, T. i. Dramatically enhanced mechanosensitivity and signal-to-noise ratio of nanoscale crack-based sensors: effect of crack depth. *Adv. Mater.* **2016**, *28* (37), 8130−8137.
(21) Wang, L.; Wu, Y.; Wang, Y.; Li, H.; Jiang, N.; Niu, K. Laterally compressed graphene foam/acrylonitrile butadiene styrene composites for electromagnetic interference shielding. *Compos. Part A: Appl. S.* **2020**, *133*, 105887.
(22) Wu, Y.; Tang, H.; Wang, L.; Zong, Y.; Jia, J.; Sun, L.; Niu, K. Temperature-insensitive stretchable conductors based on hierarchical double-layer graphene foams/PEDOT:PSS networks. *Compos. Sci. Technol.* **2023**, *242*, 110190.
(23) Wu, Y.; Wang, Z.; Liu, X.; Shen, X.; Zheng, Q.; Xue, Q.; Kim, J.-K. Ultralight graphene foam/conductive polymer composites for exceptional electromagnetic interference shielding. *ACS Appl. Mater. Interfaces* **2017**, *9* (10), 9059−9069.
(24) Favre, E. Swelling of crosslinked polydimethylsiloxane networks by pure solvents: influence of temperature. *Eur. Polym. J.* **1996**, *32* (10), 1183−1188.
(25) Liu, X.; Liu, D.; Lee, J.-h.; Zheng, Q.; Du, X.; Zhang, X.; Xu, H.; Wang, Z.; Wu, Y.; Shen, X.; et al. Spider-web-inspired stretchable graphene woven fabric for highly sensitive, transparent, wearable strain sensors. *ACS Appl. Mater. Interfaces* **2019**, *11* (2), 2282−2294.
(26) Malard, L. M.; Pimenta, M. A.; Dresselhaus, G.; Dresselhaus, M. S. Raman spectroscopy in graphene. *Phys. Rep.* **2009**, *473* (5−6), 51−87.
(27) Ferrari, A. C.; Meyer, J. C.; Scardaci, V.; Casiraghi, C.; Lazzeri, M.; Mauri, F.; Piscanec, S.; Jiang, D.; Novoselov, K. S.; Roth, S.; et al. Raman spectrum of graphene and graphene layers. *Phys. Rev. Lett.* **2006**, *97* (18), 187401.
(28) Liu, X.; Tang, C.; Du, X.; Xiong, S.; Xi, S.; Liu, Y.; Shen, X.; Zheng, Q.; Wang, Z.; Wu, Y.; et al. A highly sensitive graphene woven fabric strain sensor for wearable wireless musical instruments. *Mater. Horiz.* **2017**, *4* (3), 477−486.
(29) Liu, N.; Pan, Z.; Fu, L.; Zhang, C.; Dai, B.; Liu, Z. The origin of wrinkles on transferred graphene. *Nano Res.* **2011**, *4*, 996−1004.
(30) Yang, T.; Jiang, X.; Zhong, Y.; Zhao, X.; Lin, S.; Li, J.; Li, X.; Xu, J.; Li, Z.; Zhu, H. A wearable and highly sensitive graphene strain sensor for precise home-based pulse wave monitoring. *ACS Sens* **2017**, *2* (7), 967−974.
(31) Xu, R.; Lu, Y.; Jiang, C.; Chen, J.; Mao, P.; Gao, G.; Zhang, L.; Wu, S. Facile fabrication of three-dimensional graphene foam/poly (dimethylsiloxane) composites and their potential application as strain sensor. *ACS Appl. Mater. Interfaces* **2014**, *6* (16), 13455−13460.
(32) Tung, T. T.; Tran, M. T.; Pereira, A. L.; Cordeiro, C. M.; Nguyen, D. D.; Tai, N.-H.; Tran, V. V.; Hsu, C.-C.; Joshi, P.; Yoshimura, M.; et al. Graphene woven fabric-polydimethylsiloxane piezoresistive films for smart multi-stimuli responses. *Colloid. Surface. B* **2023**, *221*, 112940.
(33) Jeong, Y. R.; Park, H.; Jin, S. W.; Hong, S. Y.; Lee, S. S.; Ha, J. S. Highly stretchable and sensitive strain sensors using fragmentized graphene foam. *Adv. Funct. Mater.* **2015**, *25* (27), 4228−4236.
(34) Fu, X.-W.; Liao, Z.-M.; Zhou, J.-X.; Zhou, Y.-B.; Wu, H.-C.; Zhang, R.; Jing, G.; Xu, J.; Wu, X.; Guo, W.; et al. Strain dependent resistance in chemical vapor deposition grown graphene. *Appl. Phys. Lett.* **2011**, *99* (21), 213107.
(35) Zheng, Q.; Liu, X.; Xu, H.; Cheung, M.-S.; Choi, Y.-W.; Huang, H.-C.; Lei, H.-Y.; Shen, X.; Wang, Z.; Wu, Y.; et al. Sliced graphene foam films for dual-functional wearable strain sensors and switches. *Nanoscale Horiz* **2018**, *3* (1), 35−44.
(36) Li, Y.; He, T.; Shi, L.; Wang, R.; Sun, J. Strain sensor with both a wide sensing range and high sensitivity based on braided graphene belts. *ACS Appl. Mater. Interfaces* **2020**, *12* (15), 17691−17698.
(37) Na, H. R.; Lee, H. J.; Jeon, J. H.; Kim, H.-J.; Jerng, S.-K.; Roy, S. B.; Chun, S.-H.; Lee, S.; Yun, Y. J. Vertical graphene on flexible substrate, overcoming limits of crack-based resistive strain sensors. *npj Flex. Electron.* **2022**, *6* (1), 2.
(38) Chen, Y.; Zhang, Y.; Song, F.; Zhang, H.; Zhang, Q.; Xu, J.; Wang, H.; Ke, F. J. A. M. T. Graphene decorated fiber for wearable strain sensor with high sensitivity at tiny strain. *Adv. Mater. Technol.* **2021**, *6* (12), 2100421.
(39) Li, L.; Zheng, Y.; Liu, E.; Zhao, X.; Yu, S.; Wang, J.; Han, X.; Xu, F.; Cao, Y.; Lu, C.; et al. Stretchable and ultrasensitive strain sensor based on a bilayer wrinkle-microcracking mechanism. *Chem. Eng. J.* **2022**, *437*, 135399.
(40) Chu, Z.; Jiao, W.; Huang, Y.; Zheng, Y.; Wang, R.; He, X. Superhydrophobic gradient wrinkle strain sensor with ultra-high sensitivity and broad strain range for motion monitoring. *J. Mater. Chem. A* **2021**, *9* (15), 9634−9643.
(41) Liu, Q.; Chen, J.; Li, Y.; Shi, G. High-performance strain sensors with fish-scale-like graphene-sensing layers for full-range detection of human motions. *ACS Nano* **2016**, *10* (8), 7901−7906.
(42) Xue, P.; Chen, C.; Diao, D. Ultra-sensitive flexible strain sensor based on graphene nanocrystallite carbon film with wrinkle structures. *Carbon* **2019**, *147*, 227−235.
(43) Li, J.; Bao, R.; Tao, J.; Dong, M.; Zhang, Y.; Fu, S.; Peng, D.; Pan, C. Visually aided tactile enhancement system based on ultrathin highly sensitive crack-based strain sensors. *Appl. Phys. Rev.* **2020**, *7* (1), 011404.
(44) Wu, X. P.; Luo, X. M.; Chen, H. L.; Man, Y.; Bai, Y. Y.; Qin, T. Z.; Zhang, B.; Zhang, G. P. Fatigue crack-based strain sensors achieving flow detection and motion monitoring for reconnaissance robot applications. *Mater. Horiz.* **2024**, *11*, 4207.
(45) Zhu, J.; Wu, X.; Jan, J.; Du, S.; Evans, J.; Arias, A. C. Tuning strain sensor performance via programmed thin-film crack evolution. *ACS Appl. Mater. Interfaces* **2021**, *13* (32), 38105−38113.
(46) Wang, Y.; Wang, F.; Yazigi, S.; Zhang, D.; Gui, X.; Qi, Y.; Zhong, J.; Sun, L. Nanoengineered highly sensitive and stable soft strain sensor built from cracked carbon nanotube network/composite bilayers. *Carbon* **2021**, *173*, 849−856.
(47) Li, Z.-Y.; Zhai, W.; Yu, Y.-F.; Li, G.-J.; Zhan, P.-F.; Xu, J.-W.; Zheng, G.-Q.; Dai, K.; Liu, C.-T.; Shen, C.-Y. An ultrasensitive, durable and stretchable strain sensor with crack-wrinkle structure for human motion monitoring. *Chinese N. Polym. Sci.* **2021**, *39* (3), 316−326.
(48) Wang, C.; Zhao, J.; Ma, C.; Sun, J.; Tian, L.; Li, X.; Li, F.; Han, X.; Liu, C.; Shen, C.; et al. Detection of non-joint areas tiny strain and anti-interference voice recognition by micro-cracked metal thin film. *Nano Energy* **2017**, *34*, 578−585.
(49) Yang, J.; Wu, S.; Yu, J.; Deng, Y.; Qiao, F.; Zhang, K. Flexible micro-strain graphene sensors enhanced by laser-induced cracks for health monitoring. *Diam. Relat. Mater.* **2024**, *148*, 111401.
(50) Tang, C.; Xu, M.; Yi, W.; Zhang, Z.; Occhipinti, E.; Dong, C.; Ravenscroft, D.; Jung, S.-M.; Lee, S.; Gao, S.; et al. Ultrasensitive textile strain sensors redefine wearable silent speech interfaces with high machine learning efficiency. *npj Flex. Electron.* **2024**, *8* (1), 27.
(51) Wang, S.; Xiao, P.; Liang, Y.; Zhang, J.; Huang, Y.; Wu, S.; Kuo, S.-W.; Chen, T. Network cracks-based wearable strain sensors for subtle and large strain detection of human motions. *J. Mater. Chem. C* **2018**, *6* (19), 5140−5147.
(52) Ma, J.; Cheng, Z.; Tan, S.; Zheng, T.; Zong, Y. High performance strain sensor based on leather activated by micro-cracking conductive layer. *Collagen Leather* **2023**, *5* (1), 25.
(53) Cheng, X.; Cai, J.; Xu, J.; Gong, D. High-performance strain sensors based on Au/graphene composite films with hierarchical cracks for wide linear-range motion monitoring. *ACS Appl. Mater. Interfaces* **2022**, *14* (34), 39230−39239.
(54) Jeon, H.; Hong, S. K.; Kim, M. S.; Cho, S. J.; Lim, G. Omni-purpose stretchable strain sensor based on a highly dense nanocrack-

https://doi.org/10.1021/acsomega.4c10403
ACS Omega 2025, 10, 3141−3152

ing structure for whole-body motion monitoring. *ACS Appl. Mater. Interfaces* **2017**, *9* (48), 41712−41721.
(55) Wang, L.; Wu, Y.; Li, Z.; Jiang, N.; Niu, K. Wavy graphene foam reinforced elastomeric composites for large-strain stretchable conductors. *Compos. Part B: Eng.* **2021**, *224*, 109179.

https://doi.org/10.1021/acsomega.4c10403
ACS Omega 2025, 10, 3141−3152